Improved Photovoltaic Performances of Lead-Free Cs$_2$AgBiBr$_6$ Double Perovskite Solar Cells Incorporating Tetracene as Co-Hole Transport Layer

Nathan Daem, Jennifer Dewalque, Dong Kuk Kim, Gilles Spronck, Max Attwood, Jessica Wade, Catherine Henrist, Pierre Colson, Sandrine Heutz,* Rudi Cloots,* and Anthony Maho*

Cs$_2$AgBiBr$_6$ double perovskite compounds are increasingly studied in recent years as promising candidates able to counter polluting, harmful, and oxygen-/moisture-sensitive issues intrinsic to traditional lead-containing solar cells. Exhibiting high optical absorption coefficient, low toxicity, and important structural stability, Cs$_2$AgBiBr$_6$ solar cells still suffer from limited absorption of low-energy photons, low carrier mobility, and limited carrier lifetimes induced by defect states. Herein, for the first time, a molecular layer of tetracene is introduced within a Cs$_2$AgBiBr$_6$-based photovoltaic architecture: being incorporated at the interface between the double perovskite photoabsorber and spiro-OMeTAD hole transport material, tetracene allows for a suitably graded cascade of energy bands within the solar cell architecture, which ultimately improves interfacial charge transfers and reduces charge recombination. The performances in photovoltaic devices are consequently enhanced versus tetracene-free configurations, with champion values of open-circuit voltages of 1.1 V (vs. 1.0 V), current densities of 2.5 mA cm^{-2} (vs. 1.9 mA cm^{-2}), and photoconversion efficiencies of 1.7% (vs. 1.3%) with reduced hysteretic behavior.

1. Introduction

Perovskite-based solar cells (PSCs) are part of the third-generation photovoltaic (PV) technology. The current efficiency record is 25.8%,[1] making them competitive with silicon-based technologies. In the context of PV applications, lead halide compounds such as CH$_3$NH$_3$PbI$_3$ and their derivatives are the most widely used due to their low cost, tuneable direct bandgaps, high extinction coefficients, high charge carrier mobilities, and long charge carrier diffusion lengths.[2–6] However, some issues of stability and toxicity are raising concerns, motivating the drive toward new materials classes.[7,8] A new quaternary A$_2$$^+M^+$M^{3+}X$_6$$^-$ double-metal perovskite structure, which keeps the total number of valence electrons unchanged in the unit cell of 3D perovskite, has been investigated as potential lead-free light-absorbing material.[4,9] Although many possible candidates can be chosen for M$^+$ and M^{3+} cations, theoretical calculations suggest that only selected compounds with suitable decomposition enthalpy, bandgap, charge carrier dynamics/kinetics, effective mass, and exciton binding energy could be used in corresponding PV devices.[10–12] Among them, the bismuth-based Cs$_2$AgBiBr$_6$ double perovskite semiconductor is found to exhibit in principle both an indirect bandgap ($\approx$1.8 eV) and a direct bandgap ($\approx$2.2 eV), a high optical absorption coefficient, high stability, and long carrier recombination lifetimes, which make this material a very strong candidate for solar cell applications.[13,14]

N. Daem, J. Dewalque, G. Spronck, C. Henrist, P. Colson, R. Cloots, A. Maho
Group of Research in Energy and Environment from Materials (GREEnMat)
CESAM Research Unit
Chemistry Department
University of Liège
Allée du Six-Août 13, 4000 Liège, Belgium
E-mail: rcloots@uliege.be

The ORCID identification number(s) for the author(s) of this article can be found under https://doi.org/10.1002/solr.202300391.

D. K. Kim, M. Attwood, J. Wade, S. Heutz, A. Maho
Department of Materials
Imperial College London
Prince Consort Road, London SW7 2AZ, UK
E-mail: s.heutz@imperial.ac.uk

A. Maho
University of Bordeaux, CNRS, Bordeaux INP, ICMCB, UMR 5026
87 Avenue du Docteur Schweitzer, 33600 Pessac, France
E-mail: anthony.maho@icmcb.cnrs.fr

This formulation is considered among the most promising PV absorber alternatives to lead-containing compounds, notably in view of its low-toxic character and long-term moisture stability.[15] However, its range of photoconversion efficiency cannot surpass the values of standard perovskite cells due to intrinsic limitations of the compound,[16] with a theoretical efficiency being limited to 7.9%.[17] Indeed, the measured indirect bandgap of ≈ 1.8 eV, which restricts the absorption of low-energy photons in the $Cs_2AgBiBr_6$ double perovskite layer, and its carrier mobility are much lower than the one of lead halide perovskites (10 vs. 35 $cm^2 V^{-1} s^{-1}$). In addition, its actual carrier lifetimes are shorter than theoretically predicted, due to a large number of defect states at the grain boundaries in the films.[18,19]

There is therefore a strong need for improving the current efficiencies of $Cs_2AgBiBr_6$-based solar cells and corresponding promising perspectives. Indeed, the solar cell architecture can be optimized by increasing the electron and hole transfer from the photoabsorbing material to the charge transport layers, notably by incorporating at the interface a layer that can improve interfacial properties between the double perovskite and the electron transport layer (ETL; typically TiO_2) and/or hole transport layer (HTL; typically spiro-OMeTAD – 2,2′,7,7′-Tetrakis[N,N-di(4-methoxyphenyl)amino]-9,9′-spirobifluorene). Such aspects, shown to be as particularly critical in the overall PSCs literature,[20] need to also be specifically addressed for lead-free PV devices in order to improve their performances in terms of photoconversion efficiency (PCE), stability, durability, etc. For example, the use of a mesoporous TiO_2 layer (mp-TiO_2) as a co-ETL with a compact TiO_2 sublayer (c-TiO_2) has been shown to improve the transfer of electron from perovskite in numerous studies related to PSCs, including $Cs_2AgBiBr_6$ configurations.[21–24] Other reports have proposed to combine the hole transport material with interlayers made of inorganic compounds such as dyes,[22] guadinium thiocyanate (GuaSCN),[25] quantum dots, or of organic materials such as polythiophene or polyacene derivatives in "classical" lead halide PSCs.[26–31] Specifically, previous studies attempting to incorporate polyacenes as interlayer materials in perovskite architectures have led to improved interfaces between the perovskite and HTLs in terms of structural and electronic properties, resulting in reduced migration of dopants between the perovskite layer and metal electrode, particularly at elevated temperatures (>50 °C). In consequence, better charge transfer is allowed between the photoactive and charge transport layers, and a better long-term stability can therefore be expected.

Among the polyacenes, tetracene can be selected as a "co-HTL" material to be introduced at the interface between the photoactive double perovskite layer and the spiro-OMeTAD HTL. Tetracene is indeed an efficient p-type semiconductor used in many optoelectronic and photoactive devices, including lead halide PSCs as shown by Abdi-Jalebi et al.[26] In this work, as shown in the energy-level diagram of the considered PSC architecture (**Figure 1**), the highest occupied molecular orbital (HOMO) level of tetracene (−5.3 eV) stands between the HOMO levels of $Cs_2AgBiBr_6$ double perovskite (−5.9 eV) and spiro-OMeTAD (−5.2 eV), leading to a better graded cascade of energy bands. The incorporation of tetracene should therefore be able to accelerate the injection of holes from double perovskite to the spiro-OMeTAD HTL and then to the external circuit in devices. It should also limit
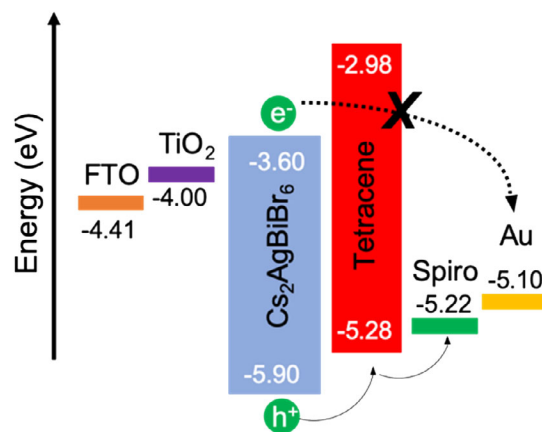
Figure 1. Energy-level diagram of the presently considered lead-free solar cells, consisting of glass/FTO/TiO_2/$Cs_2AgBiBr_6$/tetracene/spiro-OMeTAD/ Au. Band energy values are taken from other studies.[26,40]

the recombination process of the electron–hole pairs by blocking electrons from transferring toward the HTL layer and subsequently improve the PV performance of the processed PSC devices.

Therefore, in the present study, tetracene incorporation is considered through an organic molecular beam deposition (OMBD) process on a $Cs_2AgBiBr_6$ double perovskite film spray coated onto a TiO_2-covered conducting glass substrate, before being covered by spin-coated spiro-OMeTAD and evaporated Au contacts. The resulting devices reach a 1.7% photoconversion efficiency value, which leads to an improvement of 1.3 times in comparison with tetracene-free configurations (1.3%). This work shows that the incorporation of polyacene-based molecular materials with suitable energy levels is a viable route to improve hole transport and therefore PV efficiency also in lead-free perovskite devices.

2. Experimental Section

2.1. Materials and Chemicals

Fluorine-doped tin oxide (FTO)-covered glass of 2.2 mm thickness and 15 Ω sq^{-1} sheet resistance (TEC15, Greatcell Solar) was used as substrate. The following chemicals were obtained from various commercial suppliers: hydrochloric acid HCl (VWR, 37%), metallic zinc powder (Roth, ≥98%), titanium diisopropoxide bis(acetylacetonate) TAA (Sigma-Aldrich, 75 wt% in isopropanol), anhydrous ethanol EtOH (Acros, 99.5%), TiO_2 nanoparticle paste 18NR-T (Greatcell Solar), titanium chloride $TiCl_4$ (Merck, ≥97.0%), cesium bromide CsBr (Alfa Aesar, ≥99.9%), bismuth bromide $BiBr_3$ (Alfa Aesar, ≥99.0%), silver bromide AgBr (VWR, ≥99.5%), dimethylsulfoxide DMSO (Sigma-Aldrich, >99.9%), N,N'-dimethylformamide DMF (Acros Organic, 99.9%), tetracene (TCI, >97.0%), anhydrous chlorobenzene CB (Sigma-Aldrich, 99.8%), 2,2′,7,7′-Tetrakis[N,N-di(4-methoxyphenyl)amino]-9,9′-spirobifluorene – spiro-OMeTAD (Borun, >99.9%), lithium bis(trifluoromethanesulfonyl)imide Li-TFSI (Sigma-Aldrich, 99.95%), 4-tert-butylpyridine tBP (Sigma-Aldrich, 96%), anhydrous n-butanol n-BuOH (Fisher, >99.8%).

2.2. Substrate Preparation and Deposition of Electron Transport Material

First, FTO–glass substrates were cut into $2.0 \times 2.0 \, cm^2$ pieces, then etched with HCl (2 M) and metallic zinc powder to strip parts of the FTO, and prevent short circuits in the final PV cell. Substrates were cleaned over three consecutive washing steps (with soap, ethanol, and acetone, respectively) under ultrasonication before being dried under air.

A compact hole blocking layer of TiO_2 (c-TiO_2, of ≈ 30 nm thickness as previously optimized[15]) was then deposited by ultrasonic spray pyrolysis of TAA (2.2 mL) in ethanol (30.0 mL) from a Sono-Tek Exactacoat system combined with an Accumist nozzle. The following spraying parameters were used: stall power of 3.5 W, oxygen carrier gas flow of 0.9 psi, flow rate of 0.25 mL min^{-1}, nozzle speed of 100 mm s^{-1}, area spacing of 4 mm, nozzle-to-substrate distance of 5.5 cm, substrate temperature of 450 °C. The deposition pattern was repeated three times. Finally, a thermal treatment at 500 °C (ramp 100 °C h^{-1}) was performed for 30 min to crystallize TiO_2 in form of anatase phase. After cleaning treatment under UV–ozone for 15 min, a 150 nm-thick mesoporous (mp-)TiO_2 layer (as previously optimized[15]) was deposited onto the c-TiO_2 layer. Commercial TiO_2 nanoparticle paste (18NR-T, Greatcell Solar) was diluted in absolute ethanol (1:9.8 weight ratio) and spin coated at 1500 rpm for 30 s, followed by subsequent annealing at 500 °C (with a ramp of 100 °C h^{-1}) for 30 min. The mp-TiO_2 layer was immersed in an aqueous $TiCl_4$ solution (4.10^{-2} M) for 30 min at 60 °C to allow further improvement of the connectivity between the TiO_2 nanoparticles. Then, samples were successively rinsed with water and EtOH, dried with compressed air, and finally calcined for 30 min at 450 °C in a preheated oven. Before the double perovskite film deposition, a final cleaning treatment under UV–ozone for 15 min was applied to the samples.

2.3. $Cs_2AgBiBr_6$ Double Perovskite Film Preparation

A 0.15 M $Cs_2AgBiBr_6$ solution was prepared by mixing 1009.5 mg of $BiBr_3$, 422.4 mg of AgBr, and 957.6 mg CsBr in 15 mL of DMF: DMSO (4:1 volume). The solution was stirred at 80 °C overnight and was then filtered with a 0.45 μm micropore filter. As for the spray coating of the c-TiO_2 layer, the ultrasonic spray coating of the double perovskite films was performed with a Sono-Tek Exactacoat system combined with an Accumist nozzle. The following spraying parameters were used: stall power of 3.5 W, air carrier gas flow at 0.9 psi, flow rate of 0.25 mL min^{-1}, nozzle speed of 80 mm s^{-1},

area spacing of 4 mm, single pass, nozzle-to-substrate distance of 6.5 cm, substrate temperature of 150 °C. The sprayed films were finally annealed at 285 °C for 5 min (**Figure 2**).

2.4. Tetracene Film Preparation

Tetracene thin films of 120 nm thickness were processed, adapting the conditions highlighted by Abdi-Jalebi et al.[26] for optimal PSC design. Layers were grown by OMBD in a Kurt J. Lesker Spectros 100 system at a base pressure of $\approx 5 \times 10^{-7}$ mbar, from tetracene powder being evaporated at the rate of 0.5 Å s^{-1}.[32]

2.5. Solar Cell Fabrication

First, spiro-OMeTAD (186 mg) and an additive solution (84 μL) were mixed with anhydrous chlorobenzene (2 mL). The additive solution was prepared from 0.175 g Li-TFSI and 312.5 μL of *tert*-butylpyridine in 1 mL of anhydrous butanol. The solution was then deposited by spin coating at 2000 RPM for 60 s as previously optimized.[15]

After having scratched off the TiO_2/double perovskite/(tetracene/)spiro-OMeTAD layers from the photoanode contact, a gold counterelectrode layer was deposited by thermal evaporation (home-made apparatus) using a patterned mask.

2.6. Characterization

A field-emission gun microscope TESCAN CLARA under a 15-kV accelerating voltage and high vacuum was used for the morphological characterization of individual layers and assembled cells by scanning electron microscopy (SEM). All samples were coated with gold before characterization.

X-ray diffraction (XRD) was conducted in the fixed θ–2θ geometry on a Philips X'Pert Pro Panalytical instrument using a Cu Kα source ($\lambda = 1.5406$ Å) at a current of 40 A and voltage of 40 V. All references were taken from the PDF4+ database from the International Center for Diffraction Data

A Shimadzu 3600 Plus instrument with an integrating sphere (ISR-1503) was used for UV–vis–NIR spectrometry measurements.

Photoluminescence (PL) measurements were completed using a Horiba Jobin-Yvon Spex Fluorolog-3 fluorimeter instrument operated through a 405 nm excitation illuminating the top surface of the different samples.

A class A solar simulator (Newport Spectra Physics) coupled to a Keithley 2400 sourcemeter measured the PV conversion efficiency of the cells (average on 10 devices). Calibration was
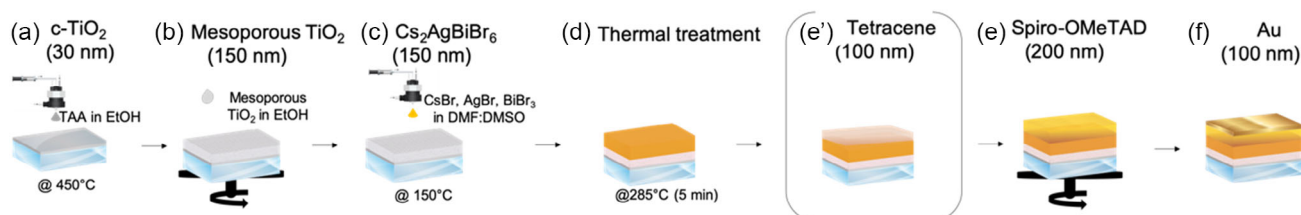
Figure 2. Overview of the manufacturing process of the $Cs_2AgBiBr_6$-based solar cells: a) spray coating of compact TiO_2 layer, b) spin coating of mesoporous TiO_2 layer, c) spray coating of $Cs_2AgBiBr_6$ layer and d) consecutive thermal treatment, e') organic molecular beam deposition of tetracene layer (when relevant), e) spin coating of spiro-OMeTAD layer, and f) evaporation of Au contacts.
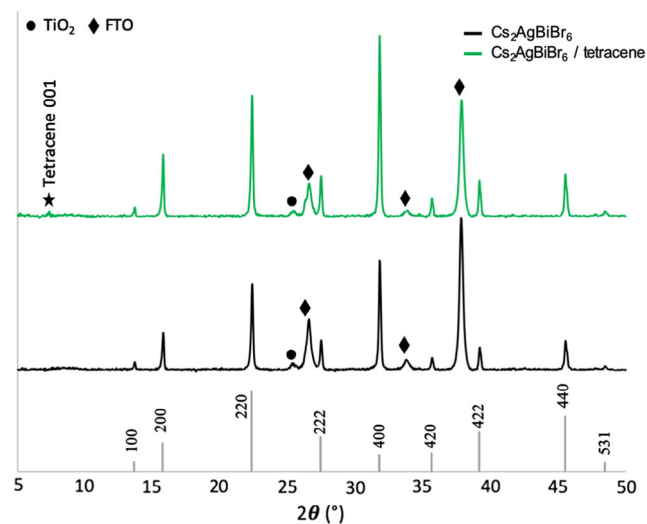
performed using a KG5-filtered silicon reference solar cell from Newport. Photocurrent density versus applied voltage curves (J–V curves) were measured on $2.0 \times 2.0 \, cm^2$ devices under simulated 1 SUN illumination (filter AM 1.5) at room temperature, using a black mask with a $0.0355 \, cm^2$ aperture (active area). Forward (0.0–1.2 V) and backward (1.2–0.0 V) measurements were performed with an increment of 4 mV ($0.2 \, s \, step^{-1}$).

For the electrochemical impedance spectroscopy (EIS), data were collected using a BioLogic SP-200 potentiostat (Science Instrument) and analyzed with the EC-Lab software. A sinusoidal potential perturbation was applied on the assembled devices and the current variation response was recorded. A frequency range of 3 MHz to 85 mHz with 10 mV sinusoidal modulation was applied for the EIS data acquisition. Measurements were performed at room temperature under standard 1 SUN illumination (AM 1.5 filter) and in open-circuit potential (OCP) conditions.

3. Results and Discussion

3.1. Structure and Morphology of $Cs_2AgBiBr_6$/Tetracene Thin Films

XRD measurements are first performed on spray-coated $Cs_2AgBiBr_6$ films before and after deposition of the tetracene layer, to evaluate the potential influence of tetracene on the $Cs_2AgBiBr_6$ crystallinity and vice versa. **Figure 3** presents the XRD patterns of the $Cs_2AgBiBr_6$ double perovskite films deposited on m-TiO_2/c-TiO_2/FTO glass substrates, with and without a tetracene top layer. Three main peaks are observed at 2θ values of

15.7°, 22.5°, and 31.8°, being representative of the (200), (220), and (400) reflections of the $Cs_2AgBiBr_6$ double perovskite cubic crystal structure, respectively. Diffraction peaks from residual $Cs_3Bi_2Br_9$ ($2\theta = 12.8°$ and 30.9°) or AgBr ($2\theta = 44.2°$), being two undesired impurity phases that can be formed during the film deposition, are not observed, which demonstrates that no chemical degradation of the double perovskite occurs after tetracene deposition.

Overall, similar diffraction peaks are observed for the $Cs_2AgBiBr_6$ layer in both configurations, with only very limited, nonsignificant differences in intensity. In order to probe a potential structural change in the $Cs_2AgBiBr_6$ films occurring after tetracene deposition, the texture factor ζ is used to normalize the experimental intensities based on simulated $Cs_2AgBiBr_6$ intensities in the same conditions of the measurements.[33] This is given by Equation (1).

$$\zeta = \frac{\iota_i \Big/ \sum_{i=0}^{i=n} \iota}{\tau_i \Big/ \sum_{i=0}^{i=n} \tau} \tag{1}$$

where ι is the experimental peak intensity and τ is the theoretical peak intensity; the sums are taken over the peaks in the 5°–45° 2θ range.

The texture factors extracted from $Cs_2AgBiBr_6$ and $Cs_2AgBiBr_6$/tetracene configurations are presented in **Table 1**. A very slight variation is observed after tetracene deposition, which indicates that it does not significantly modify the structure of the underlying double perovskite layer. The texture factors are extracted for $Cs_2AgBiBr_6$ and $Cs_2AgBiBr_6$/tetracene configurations as median values obtained from measurements on three replicates of each sample. On an average, a very slight variation is observed after tetracene deposition (see standard deviation data), which indicates that the deposition of tetracene does not significantly modify the structure of the underlying double perovskite layer. Such observation is in accordance with the work reported by Yang et al.[22] The changes induced after tetracene deposition, notably on (200), (220), and (400) diffraction peaks, are therefore considered to remain within the range of texture variation induced from spray-coating processing of the double perovskite layers (see respective standard deviation values).

Interestingly, no diffraction peaks characteristic of tetracene are intensely observed, especially the (001) reflection at $2\theta = 7.0°$ corresponding to tetracene molecules standing nearly perpendicular on the substrate (see Figure S1, Supporting Information: X-ray diffractogram of a 120 nm-thick tetracene layer deposited on a bare silicon substrate) and only very slightly noticed here. This could be due to either a lack of long-range order or to a change in the orientation of tetracene crystals from perpendicular to flat lying. That said, an increased probability that molecules lie

Figure 3. X-ray diffractograms of pristine (black) and tetracene-covered (green) $Cs_2AgBiBr_6$ films (ICDD file numbers of $Cs_2AgBiBr_6$: 01-084-8699; TiO_2: 04-011-0664; FTO: 00-005-0467).

Table 1. Texture factors of $Cs_2AgBiBr_6$ diffraction peaks present for both pristine and tetracene-covered $Cs_2AgBiBr_6$ films.

	100	200	220	222	400	420	422	440
Pristine $Cs_2AgBiBr_6$	0.85 ± 0.08	3.55 ± 0.35	0.84 ± 0.28	0.65 ± 0.26	1.34 ± 0.40	0.81 ± 0.19	0.72 ± 0.07	0.64 ± 0.03
$Cs_2AgBiBr_6$/tetracene	0.68 ± 0.01	3.23 ± 0.49	0.78 ± 0.09	0.70 ± 0.04	1.41 ± 0.05	0.88 ± 0.01	0.83 ± 0.17	0.62 ± 0.05

parallel to the substrate is generally considered as favorable from the point of view of charge transport and absorption coefficient.[34]

The morphological properties of the pristine double perovskite film (**Figure 4**A), covered with tetracene (Figure 4B) and then with spiro-OMeTAD (Figure 4C), are then analyzed
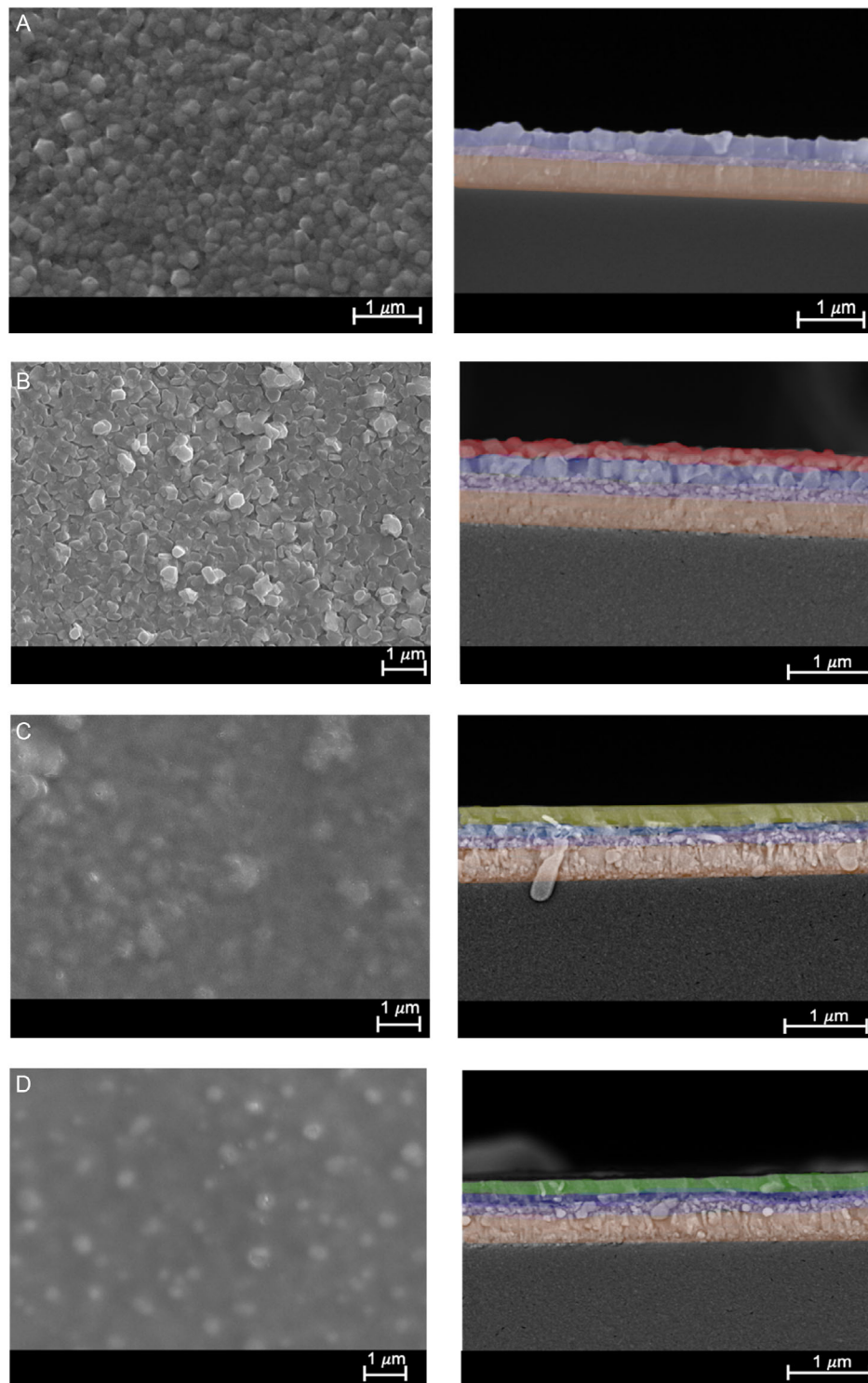

Figure 4. SEM micrographs in top-view (left) and cross-section (right) modes of A) pristine $Cs_2AgBiBr_6$, B) $Cs_2AgBiBr_6$/tetracene, C) $Cs_2AgBiBr_6$/tetracene/spiro-OMeTAD, and D) $Cs_2AgBiBr_6$/spiro-OMeTAD films. The following color code is used to label the consecutive layers: glass (grey), FTO (orange), compact-TiO_2, and mp–TiO_2 (purple) infiltrated by $Cs_2AgBiBr_6$, $Cs_2AgBiBr_6$ overlayer (blue), tetracene (red), and spiro-OMeTAD (green); the merged layer of tetracene and spiro-OMeTAD on Figure 4c is shown in olive green.

by SEM. A uniform $Cs_2AgBiBr_6$ film with lateral grain sizes of ≈160 nm is obtained by ultrasonic spray coating, showing a ≈200 nm-thick overlayer on the mp-TiO_2 layer. A ≈120 nm uniform tetracene layer is subsequently deposited, showing facetted grains with ≈300 nm lateral size; interestingly, a tetracene layer deposited on a bare silicon substrate shows grain sizes >450 nm for the same thickness (Figure S2, Supporting Information). Finally, a top layer of spiro-OMeTAD is spin coated onto tetracene, resulting in combined HTLs ensuring full coverage of the double perovskite surface. From the cross-section micrograph of the $Cs_2AgBiBr_6$/tetracene/spiro-OMeTAD stacked layers (Figure 4C), it is difficult to distinguish tetracene and spiro-OMeTAD materials, which suggests a restructuration into a ≈280 nm-thick "merged" layer being the result of the wet-based deposition of the spiro-OMeTAD material onto the precoated, vacuum-processed tetracene layer. It is noteworthy that spiro-OMeTAD deposition on a "tetracene-free" double perovskite film typically leads to ≈200 nm-thick layer (Figure 4D).

3.2. Optical Properties of $Cs_2AgBiBr_6$/Tetracene Thin Films

The absorption spectra of the spray-coated $Cs_2AgBiBr_6$ thin films before and after the deposition of the tetracene layers are reported in **Figure 5**A. As already mentioned in our previous work,[15] a strong absorption peak characteristic of $Cs_2AgBiBr_6$ is present at ≈440 nm. This spectral feature can be associated with trapped excitonic transitions below the high-energy direct bandgap intraband transitions or even color centers in the

material.[15] The absorption spectrum of the double perovskite film covered with a tetracene layer shows additional peaks at 450, 475, and 510 nm, which are attributed to the vibronic transitions in the tetracene molecules (see also the absorbance spectrum of single tetracene layers in Figure S3, Supporting Information).[26] Furthermore, considering the full wavelength range, the absorbance is globally increased when the spray-coated $Cs_2AgBiBr_6$ film is covered with the tetracene layer, which can be attributed to a higher light outcoupling[26] visually resulting in a sample with darker color (yellow vs. dark orange, see Figure S4A vs. C, Supporting Information). Similar observations can be deduced when an layer of spiro-OMeTAD layer is additionally deposited, either on pristine (tetracene-free) or on tetracene-covered double perovskite layers (Figure 5B and S4B vs. D, Supporting Information). The only difference is the apparition of a large absorption peak at ≈400 nm, which comes from the absorption induced by the spiro-OMeTAD material itself[35] and of a band at ≈700 nm related to a residual presence of lithium bis(trifluoromethanesulfonyl)imide (LiTFSI), being incorporated as an additive in the spiro-OMeTAD deposition solution.[36] Tauc plots (Figure 5C) allow for the determination of a direct bandgap of ≈2.3 eV for the double perovskite layer, which is in accordance with values previously reported in literature for similar synthesis conditions.[15] When a tetracene layer is incorporated, the bandgap value decreases to ≈2.2 eV, indicating that the tetracene may therefore reduce defects in the double perovskite layer and/or protect it from oxygen-related degradation; similar conclusions have been made by Yang et al.[22] with respect to the incorporation of a Ru-based dye interlayer.
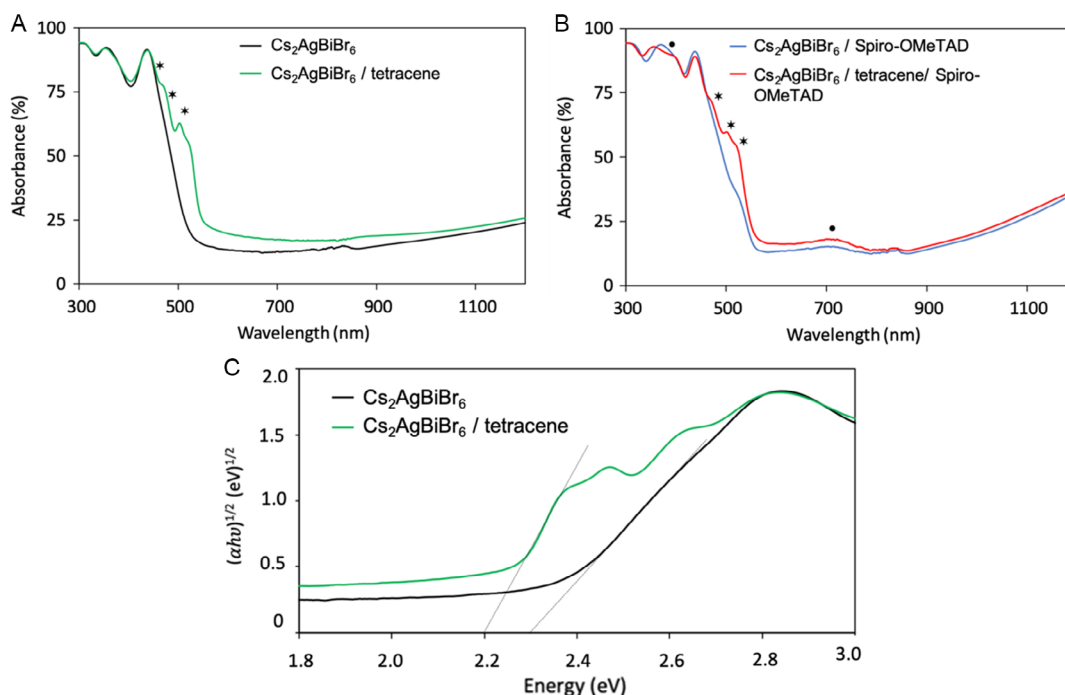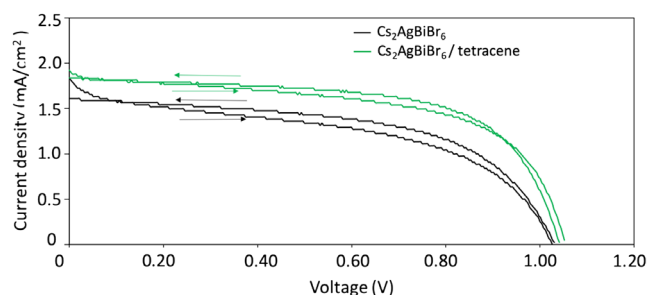

Figure 5. Absorbance spectra of A) $Cs_2AgBiBr_6$ films with/without tetracene top layer (green and black curves, respectively) and B) $Cs_2AgBiBr_6$ films with/without tetracene and spiro-OMeTAD top layers (red and blue curves, respectively), with peaks labeled with * or • being related respectively to tetracene and spiro-OMeTAD/LiTFSI. C) Tauc plots of pristine $Cs_2AgBiBr_6$ and $Cs_2AgBiBr_6$/tetracene films (black and green curves, respectively).

PL of the neat perovskite and tetracene films as well as the perovskite/tetracene bilayers has been measured by illuminating the top surface of the different samples at 405 nm. The PL spectrum (Figure S5, Supporting Information) of the perovskite/tetracene bilayers (green curve) looks very similar to the signal of the single-tetracene layers (orange curve), not showing any contribution by 600 nm that could be related to the perovskite material (black curve). This is attributed to the low absolute PL quantum yield range of the $Cs_2AgBiBr_6$ perovskite compound (especially in comparison with other lead-halide perovskite formulations[37]), being therefore undetected when associated to higher PL-responding tetracene.

3.3. Assembly and Characterization of $Cs_2AgBiBr_6$-Based Solar Cells

The PV performances of the $Cs_2AgBiBr_6$ solar cells prepared with and without introducing tetracene are evaluated (see **Figure 6**, **Table 2** and Figure S6, Supporting Information), considering the following overall architecture: glass/FTO/c-TiO_2/mp–TiO_2/$Cs_2AgBiBr_6$(/tetracene)/spiro-OMeTAD/Au (see the corresponding SEM cross-section view by Figure S7, Supporting Information). The configuration involving a tetracene layer shows champion values of 1.089 V for the open circuit voltage (average 1.064 ± 0.018 V), 2.5 mA cm^{-2} for the short circuit current density (average 2.3 ± 0.3 mA cm^{-2}), and 62% for the fill factor (average 62 ± 4%), whereas the champion device with no tetracene layer records an open circuit voltage of 1.055 V (average 1.032 ± 0.017 V), a short circuit current density of 2.2 mA cm^{-2} (average 2.0 ± 0.2), and a fill factor of 58% (average 54 ± 6%) (Figure 6, Table 2, Figure S6, Supporting Information). We have already shown in our previous study[15] that the ultrasonic spray processing of $Cs_2AgBiBr_6$ layers resulted in a significant improvement of the open-circuit voltage above 1.0 V for direct and reverse

measures, in comparison with spin-coated devices. The same trend is observed here, with the incorporation of tetracene layer further improving the current density of the device and thus highlighting better transport of electrical charges toward the electrodes, especially between the HTL and the Au contacts. Devices with tetracene also exhibit a lower hysteresis behavior than their pristine counterparts (fill factor difference between direct and reverse curves of 3 with tetracene, instead of 18 with spiro-OMeTAD only), which confirms the role of tetracene in limiting the susceptibility of ion migration.[26] Furthermore, the higher average fill factor (Figure S6, Supporting Information) in tetracene-including devices[26] can be attributed to a more efficient hole transfer in these devices as a result of the optimized hole transport energetics with graded HOMO levels of double perovskite, tetracene, and spiro-OMeTAD. All in all, the champion $Cs_2AgBiBr_6$/tetracene/spiro-OMeTAD device presents a PCE of 1.7%, while its $Cs_2AgBiBr_6$/spiro-OMeTAD counterpart presents a lower PCE value of 1.3%, highlighting the beneficial effect provided by the use of tetracene.

Even though the benefits of the tetracene incorporation on the J–V characterization and results are clearly established, with a PCE improvement of 130% (relative value), it is noteworthy that the $Cs_2AgBiBr_6$/spiro-OMeTAD benchmark devices presented here show decreased absolute efficiency values (1.3%) in comparison with results previously obtained with similar protocols, which led to higher PCE values (2.3%[15]), matching the average range of the current $Cs_2AgBiBr_6$ PSCs state of the art.[22,23,25] This difference can be explained by the deposition approach presently implemented, for which double perovskite and spiro-OMeTAD layers cannot be deposited in an uninterrupted, consecutive manner, as tetracene has to be incorporated in between through OMBD, which breaks the continuousness of the coating process of the different layers. Accordingly, in this study, the preparation of the standard "tetracene-free" configurations also involves a time break between the wet deposition of the double perovskite layer and of the spiro-OMeTAD layer. This difference in methodology is found to also impact the current density values of the samples, which are of ≈1.9–2.5 mA cm^{-2} in the present study versus ≈3.0–4.0 mA cm^{-2} in the previous one.

To further analyze the charge transfer properties of the $Cs_2AgBiBr_6$-based solar cells, EIS is conducted.[38] The EIS results are presented as Nyquist plots in **Figure 7**. Data are fitted

Figure 6. Current density–voltage (J–V) curves of champion solar cells based on $Cs_2AgBiBr_6$/spiro-OMeTAD (black) and $Cs_2AgBiBr_6$/tetracene/spiro-OMeTAD (green) configurations.
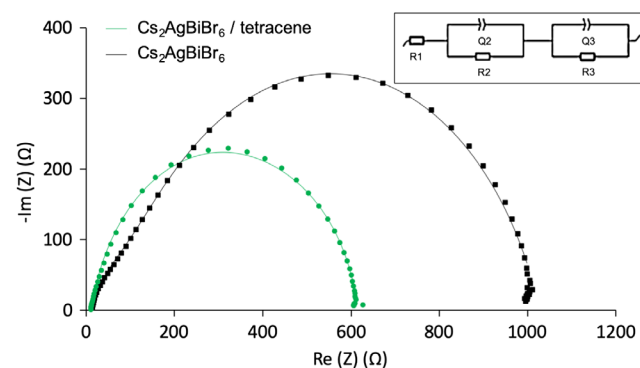
Table 2. PV parameters of the champion $Cs_2AgBiBr_6$-based devices.

		V_{oc} [V]	J_{sc} [mA cm^{-2}]	FF	PCE [%]
$Cs_2AgBiBr_6$/spiro-OMeTAD	Direct	1.018	2.2	45	1.0
	Reverse	1.082	1.9	63	1.3
$Cs_2AgBiBr_6$/tetracene/spiro-OMeTAD	Direct	1.089	2.5	62	1.7
	Reverse	1.039	2.5	65	1.7

Figure 7. EIS Nyquist plots of solar cells with $Cs_2AgBiBr_6$/spiro-OMeTAD (black) and $Cs_2AgBiBr_6$/tetracene/spiro-OMeTAD (green) configurations; inset: equivalent electrical circuit used for data fitting.

Table 3. Fitting resistance (R) and constant phase element (Q) parameters obtained from EIS data measured on the $Cs_2AgBiBr_6$-based devices.

	R_1 [Ω]	R_2 [Ω]	Q_2 [10^{-6} F s^{a-1}]	a2	R_3 [Ω]	Q_3 [10^{-6} F s^{b-1}]	a3
$Cs_2AgBiBr_6$/spiro-OMeTAD	11.0	86.9	0.435	0.763	929.5	0.510	0.786
$Cs_2AgBiBr_6$/tetracene/spiro-OMeTAD	10.0	110.5	0.990	0.938	495.1	0.202	0.840

with the equivalent circuit model shown in the inset and summarized in **Table 3**. The equivalent electrical circuit consists of resistance (R) elements and constant-phase capacitive (Q) elements: a R_1 series resistance from the current collectors, an $R_2//Q_2$ element at high frequencies for electrical processes at the interfaces, and an $R_3//Q_3$ element at low frequencies for electrochemical processes within the solar cell. The higher Q_2 and R_2 values obtained with $Cs_2AgBiBr_6$/tetracene/spiro-OMeTAD devices in comparison to the tetracene-free devices can be correlated to increased charge transfer at the interfaces and higher resistance to charge recombination and therefore result in a globally improved charge transport. Regarding R_3 and Q_3, the lower values obtained with $Cs_2AgBiBr_6$/tetracene/spiro-OMeTAD devices are indicative of a reduction of detrimental electrochemical processes, such as accumulation or depletion of ions and formation of traps in that PSC configuration. This interpretation is correlated with the higher open-circuit voltage values obtained for the $Cs_2AgBiBr_6$/tetracene/spiro-OMeTAD devices, which is known to increase with reduced traps.[39] Both high- and low-frequency EIS signatures therefore highlight the beneficial impact on charge transport of using tetracene as a co-HTL with spiro-OMeTAD in $Cs_2AgBiBr_6$-based PSCs. Complementary dark J–V measurements (Figure S8, Supporting Information) further highlight the reduction of charge recombination when tetracene is incorporated in the device architecture, which corroborates EIS measurements.

4. Conclusion

This study reports for the first time the use of tetracene as co-HTL in a lead-free PSC architecture. Incorporated between a spray-coated $Cs_2AgBiBr_6$ double perovskite layer and a spin-coated spiro-OMeTAD HTL, tetracene generates an excellent hole-extracting platform that ultimately improves the PV performances of the processed devices, with a higher PCE (1.7%) relative to the configuration without the tetracene interlayer (1.3%). The tetracene layer is shown to globally improve the charge transport due to an increased charge transfer at interfaces and a higher resistance to charges recombination, while countering the accumulation or depletion of ions and the formation of traps. In order to optimize the ultimate PV performances of the processed PSCs, one could consider to further refine the progressive energy band grading between perovskite and HTL, considering different thicknesses of tetracene-containing HTLs, in order to study the influence on hole conduction and therefore on photoconversion efficiency, as well as alternative HTL materials in combination (or not) with tetracene. The mix of wet- and vacuum-based techniques for the preparation of the different layers could also be avoided; preliminary trials of tetracene layers deposited on top of the $Cs_2AgBiBr_6$ perovskite films by spin coating of 5,12-bis((triisopropylsilyl)ethynyl)tetracene (TIPS-tetracene)

precursor (instead of tetracene deposition by vacuum-based organic OMBD) have been promisingly performed, but still need to be optimized with regard to the consecutive wet deposition of the spiro-OMeTAD layer. The presently obtained PSCs will also need to be thoroughly tested under different aging/stress conditions—relative humidity, temperature, illumination, bias—as preliminary, rough stability measurements (unshown data) seem to indicate that average PCEs of the tetracene-including devices remain stable, retaining more than 90% of the initial value after several months, while the average PCEs of tetracene-free devices lose 35% of their initial value, mostly due to a drop of V_{oc}. Finally, the use of tetracene as co-HTL with other perovskite formulations (both lead-containing or lead-free) and/or preparation approaches could be further explored: as an example, the use of hydrogenated $Cs_2AgBiBr_6$ layers, as recently highlighted by Zhang et al.[18] for its significantly enhanced PCE value (up to 6%), which would be an interesting research perspective.

Supporting Information

Supporting Information is available from the Wiley Online Library or from the author.

Conflict of Interest

The authors declare no conflict of interest.

Data Availability Statement

The data that support the findings of this study are available from the corresponding author upon reasonable request.

[1] Best Research-Cell Efficiency Chart, https://www.nrel.gov/pv/cell-efficiency.html (accessed: February 2023).
[2] D. Zhou, T. Zhou, Y. Tian, X. Zhu, Y. Tu, *J. Nanomater.* **2018**, *2018*, 1.
[3] S. D. Stranks, G. E. Eperon, G. Grancini, C. Menelaou, M. J. P. Alcocer, T. Leijtens, L. M. Herz, A. Petrozza, H. J. Snaith, *Science* **2013**, *342*, 341.
[4] R. Nie, R. R. Sumukam, S. H. Reddy, M. Banavoth, S. I. Seok, *Energy Environ. Sci.* **2020**, *30*, 2363.
[5] L. Liu, J. Lu, H. Wang, Z. Cui, G. Giorgi, Y. Bai, Q. Chen, *Mater. Rep.: Energy* **2021**, *1*, 100064.
[6] L. Song, *Mater. Rep.: Energy* **2022**, *2*, 100171.
[7] G. Schileo, G. Grancini, *J. Mater. Chem. C* **2021**, *9*, 67.
[8] H. Xiang, P. Liu, R. Ran, W. Wang, W. Zhou, Z. Shao, *Renewable Sustainable Energy Rev.* **2022**, *166*, 112614.
[9] F. Igbari, Z. K. Wang, L. S. Liao, *Adv. Energy Mater.* **2019**, *9*, 1.
[10] M. T. Hörantner, T. Leijtens, M. E. Ziffer, G. E. Eperon, M. G. Christoforo, M. D. McGehee, H. J. Snaith, *ACS Energy Lett.* **2017**, *2*, 2506.
[11] Z. Xiao, Z. Song, Y. Yan, *Adv. Mater.* **2019**, *31*, 1803792.
[12] Q. Zhang, F. Hao, J. Li, Y. Zhou, Y. Wei, H. Lin, *Sci. Technol. Adv. Mater.* **2018**, *6996*, 1.
[13] Z. Xiao, Y. Yan, *Adv. Energy Mater.* **2017**, *7*, 1.
[14] A. H. Slavney, T. Hu, A. M. Lindenberg, H. I. Karunadasa, *J. Am. Chem. Soc.* **2016**, *138*, 2138.
[15] N. Daem, J. Dewalque, F. Lang, A. Maho, G. Spronck, C. Henrist, P. Colson, S. D. Stranks, R. Cloots, *Sol. RRL* **2021**, *5*, 2100422.
[16] F. H. Alharbi, S. Kais, *Renewable Sustainable Energy Rev.* **2015**, *43*, 1073.
[17] C. N. Savory, A. Walsh, D. O. Scanlon, *ACS Energy Lett.* **2016**, *1*, 949.
[18] Z. Zhang, Q. Sun, Y. Lu, F. Lu, X. Mu, S. H. Wei, M. Sui, *Nat. Commun.* **2022**, *13*, 1.
[19] X. Yang, H. Xiang, C. Zhou, R. Ran, W. Wang, W. Zhou, Z. Shao, *J. Colloid Interface Sci.* **2022**, *628*, 476.
[20] Y. Yu, J. Xia, Y. Liang, *AIP Adv.* **2022**, *12*, 055307.
[21] E. Greul, M. L. Petrus, A. Binek, P. Docampo, T. Bein, *J. Mater. Chem. A* **2017**, *5*, 19972.
[22] X. Yang, Y. Chen, P. Liu, H. Xiang, W. Wang, R. Ran, W. Zhou, Z. Shao, *Adv. Funct. Mater.* **2020**, *30*, 1.
[23] D. Zhao, C. Liang, B. Wang, T. Liu, Q. Wei, K. Wang, H. Gu, S. Wang, S. Mei, G. Xing, *Energy Environ. Mater.* **2022**, *5*, 1317.
[24] S. Miao, S. Yuan, D. Zhu, Q. Cai, H. Y. Wang, Y. Wang, Y. Qin, X. C. Ai, *Phys. Chem. Chem. Phys.* **2022**, *24*, 20689.
[25] X. Yang, A. Xie, H. Xiang, W. Wang, R. Ran, W. Zhou, Z. Shao, *Appl. Phys. Rev.* **2021**, *8*, 1ENG.
[26] M. Abdi-Jalebi, M. I. Dar, S. P. Senanayak, A. Sadhanala, Z. Andaji-Garmaroudi, L. M. Pazos-Outón, J. M. Richter, A. J. Pearson, H. Sirringhaus, M. Grätzel, R. H. Friend, *Sci. Adv.* **2019**, *5*, 1.
[27] S. Kazim, F. J. Ramos, P. Gao, M. K. Nazeeruddin, M. Grätzel, S. Ahmad, *Energy Environ. Sci.* **2015**, *8*, 1816.
[28] K. Wang, Y. Huang, R. Chen, Z. Xu, *Appl. Surf. Sci.* **2016**, *388*, 376.
[29] H. S. Kim, J. H. Park, W. H. Lee, H. H. Kim, Y. D. Park, *Soft Matter* **2019**, *15*, 7369.
[30] D. A. Kadri, D. A. Karim, M. Seck, K. Diouma, P. Marcel, *Mater. Sci. Appl.* **2018**, *09*, 900.
[31] A. R. Bowman, S. D. Stranks, B. Monserrat, *Chem. Mater.* **2022**, *34*, 4865.
[32] M. Attwood, D. K. Kim, J. H. L. Hadden, A. Maho, W. Ng, H. Wu, H. Akutsu, A. J. P. White, S. Heutz, M. Oxborrow, *J. Mater. Chem. C* **2021**, *9*, 17073.
[33] D. K. Kim, S. Lubert-Perquel, S. Heutz, *Mater. Horiz.* **2020**, *7*, 289.
[34] S. B. Jo, H. H. Kim, H. Lee, B. Kang, S. Lee, M. Sim, M. Kim, W. H. Lee, K. Cho, *ACS Nano* **2015**, *9*, 8206.
[35] A. Krishna, D. Sabba, J. Yin, A. Bruno, L. J. Antila, C. Soci, S. Mhaisalkar, A. C. Grimsdale, *J. Mater. Chem. A* **2016**, *4*, 8750.
[36] W. Zhang, L. Wang, Y. Guo, B. Zhang, V. Leandri, B. Xu, Z. Li, J. M. Gardner, L. Sun, L. Kloo, *Chem. Commun.* **2020**, *56*, 1589.
[37] G. Longo, S. Mahesh, L. R. V. Buizza, A. D. Wright, A. J. Ramadan, M. Abdi-Jalebi, P. K. Nayak, L. M. Herz, H. J. Snaith, *ACS Energy Lett.* **2020**, *5*, 2200.
[38] E. Von Hauff, D. Klotz, *J. Mater. Chem. C* **2022**, *10*, 742.
[39] T. Kirchartz, *Philos. Trans. R. Soc., A* **2019**, *377*, 20180286.
[40] X. Yang, W. Wang, R. Ran, W. Zhou, Z. Shao, *Energy Fuels* **2020**, *34*, 10513.